Lattice-Rotation Vortex at the Charged Monoclinic Domain Boundary in a Relaxor Ferroelectric Crystal

Yu-Tsun Shao[1] and Jian-Min Zuo[1,2,*]

[1]*Department of Materials Science and Engineering, University of Illinois at Urbana-Champaign, Urbana, Illinois 61801, USA*
[2]*Frederick Seitz Materials Research Laboratory, University of Illinois at Urbana-Champaign, Urbana, Illinois 61801, USA*

We present evidence of lattice-rotation vortices having an average radius of $\sim$7 nm at the ferroelectric domain boundary of $(1\text{-}x)\text{Pb}(\text{Zn}_{1/3}\text{Nb}_{2/3})\text{O}_3\text{-}x\text{PbTiO}_3$ ($x = 0.08$). Maps of crystal orientations and domain symmetry breaking are obtained using scanning convergent beam electron diffraction, which show fractional rotation vortices near the 50° monoclinic domain walls. The merging of 2D and 1D topological defects is consistent with inhomogeneous boundary charge and expected to have a large impact on the domain-switching mechanisms in relaxor ferroelectric crystals and ferroelectric devices.

Topological defects, such as ferroelectric domain walls (DWs), exhibit emergent physical properties with potential applications in electronic devices. For example, charged DWs of BiFeO_3 [1] and $\text{Pb}(\text{Zr}, \text{Ti})\text{O}_3$ [2] exhibit a significant conductivity increase compared to bulk materials, which is movable and can be advantageous for device applications [3]. DWs involve a change in the polarization direction and small lattice distortions. Having a large density of mobile DWs also facilitates domain switching and therefore dramatically enhances the susceptibility of ferroelectrics and piezoelectric coupling coefficients [4].

Extensive studies of ferroelectric domains by microscopy [5,6] and diffraction [7–18] have demonstrated that ferroelectric DWs can be categorized by the dipole transition behaviors across the boundary, which are nonchiral DWs (Ising-like), chiral DWs (Bloch- or Néel-like), or mixtures of both [19]. However, recent atomic resolution electron imaging revealed polarization rotation vortex in tetragonal $\text{Pb}(\text{Zr}, \text{Ti})\text{O}_3$ [20,21], rhombohedral BiFeO_3 [22] crystals, and the superlattices of SrTiO_3 and PbTiO_3 [23,24]. Furthermore, in lead-based complex perovskite oxides having the chemical formula $(1\text{-}x)\text{Pb}(B'^{+2}_{1/3}B''^{+5}_{2/3})\text{O}_{3\text{-}x}\text{-}x\text{Pb}(B'''^{+4})\text{O}_3$ (B', B'', $B''' = $ Zn, Nb, Ti for PZN-PT, and Mg, Nb, Ti for PMN-PT), exceptional piezoelectric properties [25] are obtained at the morphotropic phase boundary (MPB), where nanometer-sized monoclinic domains have been reported by x-ray diffraction [5,26], neutron diffraction [11–15], and electron microscopy [16,18,25]. On the other hand, we know little about the structure and properties of DWs in monoclinic crystals. Theory predicts mechanically permissible but slightly charged DWs parallel to {100} or {110} planes in addition to 180° DWs [27,28]. The structural determination of DWs in general requires (1) identifying two neighboring polarization domains, (2) determining the transition structure between the domains, and (3) identifying the nature of the polarization in the transition region.

All three tasks are experimentally difficult for determining monoclinic and nanometer-sized domains, and consequently, it was experimentally challenging to study in relaxor ferroelectrics the coupling between electric dipoles and strain, which can induce chirality at the DWs [29].

Here, we describe a scanning convergent beam electron diffraction (SCBED) study of the DWs in the relaxor-based ferroelectric crystal of PZN-8%PT. Using energy-filtered (EF) SCBED, we have identified nm-sized domains having monoclinic (M) Pm symmetry in single crystal PZN-8% PT. A careful examination of the DWs revealed the presence of lattice-rotation vortices near DWs. These vortices involve continuous lattice rotation across length scales of $\sim$15 nm in diameter.

Single crystal PZN-8%PT (unpoled flux-grown single crystal, Microfine Materials Technologies Pte. Ltd., Singapore) was selected for study. Thin crystals were prepared along pseudocubic axes of $[100]_C$, $[001]_C$, and $[111]_C$ (C for pseudocubic axes) using the method described previously [30]. The same sample preparation procedure was applied successfully for the determination of symmetry in single crystal BaTiO_3 [31].

The principle of domain identification is based on CBED determination of crystal symmetry. A focused electron probe is rastered across a region of the sample and used to record diffraction patterns. Because of the convergent beam, the diffracted beam appears as a disk instead of a sharp diffraction spot, and CBED has the spatial resolution ranging from a few to hundreds of nanometers [32–34]. The crystal point group can be obtained at different sample points by careful study of 2D features in transmitted disk and diffracted disks. Specifically, the ferroelectric polarization direction, which lies in the mirror plane, can be determined from multiple scattering effects for certain incident beam directions. Thus, ferroelectric domains can be identified by the change of CBED pattern symmetry (Fig. 1). For example, the mirror direction can be used to
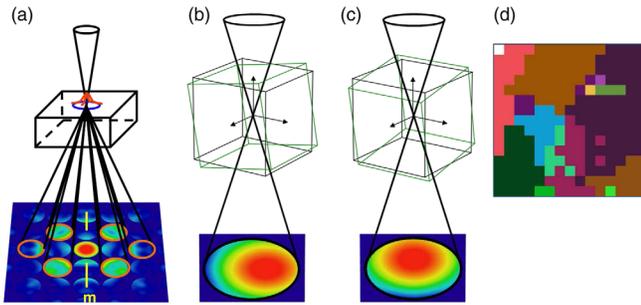
FIG. 1. *Principles of using CBED for determining mirror symmetry and crystal rotation.* Figure (a) shows an example for the mirror symmetry quantification, while crystal rotation along the x and y axes leads to a shift in the center of the CBED (000) pattern as shown in (b) and (c). The average of the cross-correlation coefficients of three pairs of discs labeled in orange in (a) is taken as $\gamma_{m,\text{average}}$, whose values are shown in (d) for a scan of 15×15 points or 225 CBED patterns. Here, each color represents a different CBED pattern, whereas similar CBED patterns are shown in the same color.

determine the 60° domains in PMN-31%PT with the aid of dynamic diffraction simulation using the Bloch wave method [25,35]. The change in CBED pattern symmetry is quantified using the normalized cross-correlation (γ_m) value of a pair of diffraction discs related by mirror symmetry using the algorithm previously proposed by Kim *et al.* [36]. For convenience of having just one γ_m value for one CBED pattern, the γ_m values of three pairs of discs with the highest intensity were averaged, noted as $\gamma_{m,\text{average}}$ shown in Fig. 1(a). By scanning the electron probe over a region of crystals and recording and quantifying CBED patterns for scanning CBED, the crystal symmetry can be mapped. Figure 1(d) shows an example. CBED patterns of different $\gamma_{m,\text{average}}$ values are indicated by different colors in Fig. 1(d) [25].

For determining the crystal rotation, we use the BF disk (transmitted beam) of CBED, which possesses the center of symmetry belonging to the Laue diffraction group according to Buxton *et al.* [32]. The location of the center of symmetry changes when crystal rotates as illustrated in Figs. 1(b) and 1(c).

The SCBED experiments were carried out using a JEOL 2010F FEG TEM operated at 200 kV with a convergent beam of 2.6 nm in FWHM (full width at half maximum). Energy filtering (EF), which improves the contrast of CBED patterns, was performed using a Gatan imaging filter (GIF). EF-SCBED was performed by scanning the focused electron probe over a selected area on a 15×15 grid, step size of 2 nm, and through a postcolumn GIF energy window of 10 eV. The shift and tilt of diffraction patterns during beam scanning were minimized and calibrated using a silicon single crystal [37]. Following the procedures described in [35], the symmetry of PZN-8%PT was determined as monoclinic *Pm*, which agrees with the x-ray diffraction result [12].

Nanodomains are observed using EF-SCBED. Symmetry variations across these domains in three EF-SCBED datasets from three different sample areas are shown in Figs. 2(a), 2(b), and 2(c). The scan consists of 15 by 15 points, with a step size of 2 nm. The $\gamma_{m,\text{average}}$ of the representative CBED patterns in each region are shown in grayscale. We identified type-1 and type-2 nanodomains with different mirror symmetry. The boundaries between these two domains are indicated as dashed lines in the figures.

We noticed that the center-of-mass of the intensity distribution within the BF disc of each pattern in the EF-SCBED dataset is not always located at the exact center. This observation could have two possible explanations: microscope optics and local crystal tilting. First, the hysteresis in the scanning coils or the lens in the microscope could lead to imperfect optical alignment while scanning the beam, which results in an effective beam tilt and a consequent intensity redistribution in the BF disc. Second, if the crystal is not oriented on the exact zone axis, this small angular deviation could also lead to an intensity redistribution in the BF disc. This is shown schematically in Figs. 1(b) and 1(c). If small bending or buckling exists during specimen preparation, the intensity redistribution in the BF disc would mainly be shifting in a way consistent with bending. We excluded the effects of microscope optics by performing EF-SCBED on a Si single crystal. This measurement defines the maximum electron beam tilt and the lattice rotation measurement precision at ±0.012 degrees. In an effort to quantify how much the crystal is deviated from the exact zone axis, we calculated the displacements (in pixels) of the center-of-mass of each BF disc and converted these displacements into crystal rotations (in degrees).

By measuring the shift in the BF disc of a CBED pattern using this method, we determined the rotation of the crystal and represented this rotation as a vector over nanometer-sized sample regions. The vector at each data point indicates the crystal rotation averaged over a volume of ~280 nm^3. Figures 3(a), 3(b), and 3(c) show the crystal rotation map derived from the same EF-SCBED datasets as Figs. 2(a), 2(b), and 2(c), respectively. Figure 3(a) shows a
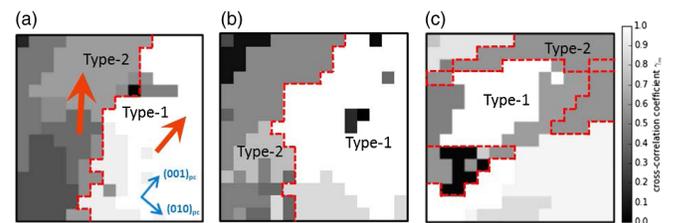
FIG. 2. *Distribution of two nanodomains using SCBED.* (a), (b), and (c) map out the $\gamma_{m,\text{average}}$ variations across two types of domains. The red dashed line indicates the domain boundary. The orange arrows indicate the projected polarization directions for each type of domain.
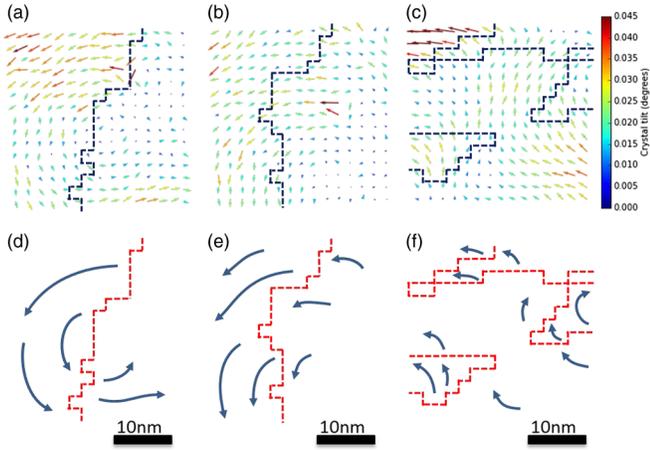
FIG. 3. *Maps of distribution of two nanodomains and lattice rotation vortices.* Figures (a), (b), and (c) show the crystal rotation at each pixel, superimposed with the domain walls indicated by the blue dashed lines. Figures (d), (e), and (f) illustrates how the crystal rotates across the domain boundaries schematically.

FIG. 4. *Experimental and simulated CBED patterns along various zone axes.* The mirror plane in the (a) type-1 and (b) type-2 domains is rotated by 45°. Figures (c) and (d) show simulated patterns of M_C (Pm) using the Bloch wave method and corresponding to the experimental (a) and (b) patterns, respectively. The indexing is based on simulated diffraction patterns.

vortexlike pattern with the vortex center near the domain boundary and a radius of curvature of ∼7 nm calculated from the discrete points. On the other hand, the vortex feature is not as distinct in Figs. 3(b) and 3(c). The continuous crystal rotation is shown schematically in Figs. 3(d), 3(e), and 3(f).

The type-1 and type-2 domains identified in Fig. 2 are associated with two distinguishable CBED patterns that were observed along the $[100]_C$ incident direction [Figs. 4(a) and 4(b)]. Figures 2(a), 2(b), and 2(c) show the symmetry maps where these two patterns were detected. The highest γ_m values of type-1 and type-2 patterns are detected along two different directions (A and B) as shown in Figs. 4(a) and 4(b). The A and B directions are rotated by 45° along the $[100]_C$ zone axis. The corresponding simulated patterns for type-1 and type-2 domains are along monoclinic Pm zone axis $[100]_{Pm}$ and $[010]_{Pm}$, as shown in Figs. 4(c) and 4(d), respectively. In the Pm structure model, the polarization direction is $\vec{P}_S = [u, 0, v]_{Pm} = [3, 0, 4]_{Pm}$, which lies in the mirror plane of Pm symmetry [12]. Along the $[100]_{Pm}$ incident direction, the mirror plane is superimposed on $(001)/(00\bar{1})$ reflections, which is parallel to the A direction in Fig. 4(a). This mirror is not observed along the $[010]_{Pm}$ incident direction. The projection of the polarization lies approximately on the $(101)/(\bar{1}0\bar{1})$ reflections, which is parallel to the B direction in Fig. 4(b). The highest mirror symmetry in this case is detected along direction B in the simulated pattern [Fig. 4(d)] with $\gamma_{m,\text{simulated}} = 60\%$.

Quantification of mirror symmetry for Figs. 4(a) and 4(b) gives $\gamma_{m,A}^1 = 95\%$ and $\gamma_{m,A}^2 = 34\%$, respectively. (The superscript indicates the domain type, and the subscript denotes the mirror plane direction.) This shows that the

mirror plane of type-1 domains is along the A direction. For the type-2 domains, a good match is obtained with $[010]_{Pm}$. The γ_m value along the B direction of the recorded patterns roughly agrees with the simulated value, with $\gamma_{m,\text{experimental}} = 54\%$.

Based on the best matching structural model of Pm, the orientation relationship between the type-1 and 2 nanodomains with respect to the pseudocubic axes is shown schematically in Fig. 5. For type-1 domains, which belong to the $[100]_{Pm}$ zone axis, the monoclinic axes of a_{Pm} and b_{Pm} are along $[100]_{PC}$ and $[010]_{PC}$, respectively. The c_{Pm} is slightly deviated away from the $[001]_{PC}$ direction with an angle $(90° - \beta)$ in the $a_{Pm} - c_{Pm}$ plane. Type-2 domains belong to the $[010]_{Pm}$ zone axis, for which the monoclinic axes of a_{Pm} and b_{Pm} are rotated by 90° with respect to the cubic c-axis. If converting the two polarization directions $[3, 0, 4]_{Pm}$ and $[0, 3, 4]_{Pm}$ from fractional coordinates into Cartesian coordinates, the polarization directions in Cartesian coordinates would be [3.03, 0.02, 4.05] and [0.02, 3.01, 4.05], respectively. The angle between the two vectors is 50°. The presence of 50° polarization domains is also evidence which excludes the tetragonal (T) or rhombohedral (R) symmetries, since this type of domain is only permitted in crystals with orthorhombic or lower symmetries [27,28]. Bokov and Ye considered mechanically permissible domain configurations with monoclinic Pm symmetry. We observed regions with high symmetry, which implies no overlapping of 1/2 type domains. However, we cannot exclude the overlapping of 2/4 domains in high symmetry region [28].
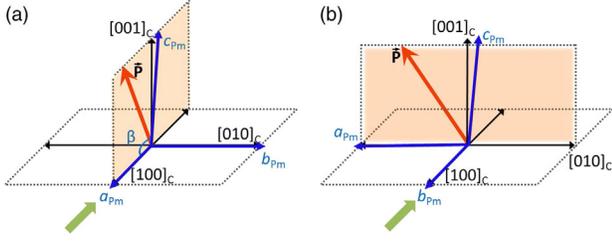
FIG. 5. *Orientation relationship between two nanodomains with respect to the pseudocubic axes.* Figures (a) and (b) correspond to type-1 and type-2 domains, respectively.

FIG. 6. *Schematic diagrams of various types of polarization vortices.* The reported (a) flux-closure quadrants in a thin ferroelectric film embedded in a dielectric matrix, (b) dipole vortex-anti-vortex pairs in a very thin ferroelectric film, (c) 180° charged domain wall, and (d) our observation of 50° monoclinic charged domain wall. E_1 and E_2 represents the inhomogeneous electric field in type-1 and type-2 domains, respectively.

Vortices form in ferroelectric crystals by two different mechanisms. Figure 6(a) shows flux-closure domain patterns associated with continuous dipole rotations have been reported in ferroelectric thin films [21–24,36] or ferroelectric nanodots [38–40]. These patterns involve continuous dipole rotations near the vertices of triangular or quadrantal domain boundaries. By reducing the thickness of the thin film, ferroelectric dipole vortex-antivortex pairs can be stabilized [24], as shown in Fig. 6(b). The continuous rotation of the dipoles in vortex structures can also result from depolarizing fields, which are created by incompletely compensated charges at the surfaces and interfaces [Fig. 6(c)]. Experimental evidence for a continuous rotation of the dipoles was reported by Jia *et al.* [20,21] in Pb(Zr, Ti)O$_3$ at the 180° domain walls. The organization of dipoles in vortex structures reduces depolarizing fields.

The rotation we observed is part of the lattice deformation matrix with displacement vector $\boldsymbol{u}(\vec{r})$, defined by rigid body rotation tensor $\tilde{w}_{ij} = \frac{1}{2}(e_{ij} - e_{ji})$, where the strain tensor is $\varepsilon_{ij} = \frac{1}{2}(e_{ij} + e_{ji})$ and the quantity $e_{ij} = (\partial u_i / \partial x_j)$. For relaxor ferroelectric crystals with monoclinic symmetry, disinclination exists between two domains with an angular mismatch determined by unit cell parameters [28,41]. Strain accompanies the polarization rotation due to the strong electromechanical coupling [9,10,42]. We speculate that the crystal rotation vortex can be a result of accommodating disinclination strain and charge discontinuity. First, the disinclination strain can be estimated by calculating Lagrangian finite strain tensors [43]. The maximum strain between neighboring type-1 and type-2 unit cells [Fig. 5] calculated using lattice parameters is 1.3%, which is comparable to the 1.5% strain at the vertex core of rhombohedral BiFeO$_3$ [44]. However, the 1.3% strain is relaxed by a continuous lattice rotation over 15 nm, the diameter of the lattice rotation vortex.

Second, the depolarizing fields and effects on local dipoles can be simplified by considering the polarization of adjacent domains since $\vec{\Delta} \cdot \vec{P} = \rho_b$, where ρ_b is the bound charge density, and $\vec{\tau} = \vec{P} \times \vec{E}$, which is the torque acting on the dipoles by the depolarization field. At 180° charged DWs, the depolarization fields induced by bound charge are symmetrical and the forces on the dipoles are

opposite on the two sides of the DWs, which creates a flux-closure vortex. However, this symmetry is broken in the case of a slightly charged monoclinic 50° DW, as shown in Fig. 6(d). The magnitude of inhomogeneous electric fields, E_1 and E_2 in type-1 and type-2 domains, respectively, are different due to strong dielectric anisotropy of the crystal [42]. This torque is also strongest when $\vec{P}$ is normal to $\vec{E}$, and this torque is weak in the type-I domain because its $\vec{P}$ is pointing out of plane. This is consistent with our observation shown in Figs. 3(a) and 3(b), which the average magnitude of lattice rotation in type-2 domains is larger than that of in type-1 domains.

The above observation raises important questions about the roles of the lattice rotation vortex in domain switching in ferroelectric systems. Previously, first-principles calculations have predicted an intermediate state having a coexisting toroidal moment and out-of-plane-polarization in ferroelectric nanoparticles [45,46]. The occurrence of lattice rotation vortices at the ferroelectric domain walls suggests the interaction between 2D and 1D topological defects. An analogy can be made with the presence of magnetic vortices, known as Skyrmions. The interplay between spin, orbital, charge, and strain degrees of freedom associated with Skyrmions suggests a complex landscape of topological defects in ferroelectrics that may be explored for new applications and functionalities.

In conclusion, we observed local crystal rotation vortex at the 50° monoclinic domain boundary. The fractional crystal rotation vortex is attributed to depolarization fields due to charge discontinuity across the domain walls and their forces on local dipoles.

———————————

*Corresponding author.
jianzuo@illinois.edu

[1] W.-F. Rao and Y. U. Wang, Appl. Phys. Lett. **90**, 041915 (2007).
[2] J. Seidel, L. W. Martin, Q. He, Q. Zhan, Y.-H. Chu, A. Rother, M. E. Hawkridge, P. Maksymovych, P. Yu, M. Gajek, N. Balke, S. V. Kalinin, S. Gemming, F. Wang, G. Catalan, J. F. Scott, N. A. Spaldin, J. Orenstein, and R. Ramesh, Nat. Mater. **8**, 229 (2009).
[3] J. Guyonnet, I. Gaponenko, S. Gariglio, and P. Paruch, Adv. Mater. **23**, 5377 (2011).
[4] C. Catalan, J. Seidel, R. Ramesh, and J. F. Scott, Rev. Mod. Phys. **84**, 119 (2012).
[5] A.-E. Renault, H. Dammak, G. Calvarin, M. P. Thi, and P. Gaucher, Jpn. J. Appl. Phys. **41**, 3846 (2002).
[6] M. Abplanalp, D. Barošová, P. Bridenbaugh, J. Erhart, J. Fousek, P. Günter, J. Nosek, and M. Šulc, J. Appl. Phys. **91**, 3797 (2002).
[7] D. E. Cox, B. Noheda, G. Shirane, Y. Uesu, K. Fujishiro, and Y. Yamada, Appl. Phys. Lett. **79**, 400 (2001).
[8] D. La-Orauttapong, B. Noheda, Z.-G. Ye, P. M. Gehring, J. Toulouse, D. E. Cox, and G. Shirane, Phys. Rev. B **65**, 144101 (2002).
[9] B. Noheda, D. E. Cox, G. Shirane, S.-E. Park, L. E. Cross, and Z. Zhong, Phys. Rev. Lett. **86**, 3891 (2001).
[10] B. Noheda, Z. Zhong, D. E. Cox, G. Shirane, S-E. Park, and P. Rehrig, Phys. Rev. B **65**, 224101 (2002).
[11] J. S. Forrester and E. H. Kisi, Acta Crystallogr. Sect. C **63**, i115 (2007).
[12] J.-M. Kiat, Y. Uesu, B. Dkhil, M. Matsuda, C. Malibert, and G. Calvarin, Phys. Rev. B **65**, 064106 (2002).
[13] E. H. Kisi and J. S. Forrester, J. Phys. Condens. Matter **20**, 165208 (2008).
[14] K. Ohwada, K. Hirota, P. W. Rehrig, P. M. Gehring, B. Noheda, Y. Fujii, S.-E. Park, and G. Shirane, J. Phys. Soc. Jpn. **70**, 2778 (2001).
[15] K. Ohwada, K. Hirota, P. W. Rehrig, Y. Fujii, and G. Shirane, Phys. Rev. B **67**, 094111 (2003).
[16] T. Asada, T. Shibata, and Y. Koyama, Ferroelectrics **347**, 17 (2007).
[17] K.-H. Kim, D. A. Payne, and J.-M. Zuo, Appl. Phys. Lett. **97**, 261910 (2010).
[18] J.-K. Lee, J. Y. Yi, K.-S. Hong, S.-E. Park, and J. Millan, J. Appl. Phys. **91**, 4474 (2002).
[19] D. Lee, R. K. Behera, P. Wu, H. Xu, Y. L. Li, S. B. Sinnott, S. R. Phillpot, L. Q. Chen, and V. Gopalan, Phys. Rev. B **80**, 060102 (2009).
[20] C.-L. Jia, S.-B. Mi, K. Urban, I. Vrejoiu, M. Alexe, and D. Hesse, Nat. Mater. **7**, 57 (2008).
[21] C.-L. Jia, K. W. Urban, M. Alexe, D. Hesse, and I. Vrejoiu, Science **331**, 1420 (2011).
[22] C. T. Nelson, B. Winchester, Y. Zhang, S.-J. Kim, A. Melville, C. Adamo, C. M. Folkman, S.-H. Baek, C.-B. Eom, D. G. Schlom, L.-Q. Chen, and X. Pan, Nano Lett. **11**, 828 (2011).
[23] Y. L. Tang, Y. L. Zhu, X. L. Ma, A. Y. Borisevich, A. N. Morozovska, E. A. Eliseev, W. Y. Wang, Y. J. Wang, Y. B. Xu, Z. D. Zhang, and S. J. Pennycook, Science **348**, 547 (2015).
[24] A. K. Yadav, C. T. Nelson, S. L. Hsu, Z. Hong, J. D. Clarkson, C. M. Schlepütz, A. R. Damodaran, P. Shafer, E. Arenholz, L. R. Dedon, D. Chen, A. Vishwanath, A. M. Minor, L. Q. Chen, J. F. Scott, L. W. Martin, and R. Ramesh, Nature (London) **530**, 198 (2016).
[25] K.-H. Kim, D. A. Payne, and J.-M. Zuo, Appl. Phys. Lett. **107**, 162902 (2015).
[26] R. Bertram, G. Reck, and R. Uecker, J. Cryst. Growth **253**, 212 (2003).
[27] J. Sapriel, Phys. Rev. B **12**, 5128 (1975).
[28] A. A. Bokov and Z.-G. Ye, J. Appl. Phys. **95**, 6347 (2004).
[29] B. Houchmandzadeh, J. Lajzerowicz, and E. Saljie, J. Phys. Condens. Matter **3**, 5163 (1991).
[30] M. Schaffer, B. Schaffer, and Q. Ramasse, Ultramicroscopy **114**, 62 (2012).
[31] Y.-T. Shao and J.-M. Zuo, Microsc. Microanal. **22 (Suppl 3)**, 516 (2016).
[32] B. F. Buxton, J. A. Eades, J. W. Steeds, and G. M. Rackham, Phil. Trans. R. Soc. A **281**, 171 (1976).
[33] M. Tanaka, Acta Crystallogr. Sect. A **50**, 261 (1994).
[34] J. P. Morniroli and J. W. Steeds, Ultramicroscopy **45**, 219 (1992).
[35] K.-H. Kim, D. A. Payne, and J.-M. Zuo, Phys. Rev. B **86**, 184113 (2012).
[36] K.-H. Kim and J.-M. Zuo, Ultramicroscopy **124**, 71 (2013).
[37] K.-H. Kim, H. Xing, J.-M. Zuo, P. Zhang, and H. Wang, Micron **71**, 39 (2015).
[38] A. Gruverman, D. Wu, H.-J. Fan, I. Vrejoiu, M. Alexe, R. J. Harrison, and J. F. Scott, J. Phys. Condens. Matter **20**, 342201 (2008).
[39] M. J. Polking, M.-G. Han, A. Yourdkhani, V. Petkov, C. F. Kisielowski, V. V. Volkov, Y. Zhu, G. Caruntu, A. P. Alivisatos, and R. Ramesh, Nat. Mater. **11**, 700 (2012).
[40] A. Schilling, D. Byrne, G. Catalan, K. G. Webber, Y. A. Genenko, G. S. Wu, J. F. Scott, and J. M. Gregg, Nano Lett. **9**, 3359 (2009).
[41] J. Přívratská, Ferroelectrics **291**, 197 (2003).
[42] S.-E. Park and T. R. Shrout, J. Appl. Phys. **82**, 1804 (1997).
[43] M. I. Aroyo, J. M. Perez-Mato, D. Orobengoa, E. Tasci, G. de la Flor, and A. Kirov, Bulg Chem Commun **43**, 183 (2011).
[44] N. Balke, B. Winchester, W. Ren, Y. H. Chu, A. N. Morozovska, E. A. Eliseev, M. Huijben, R. K. Vasudevan, P. Maksymovych, J. Britson, S. Jess, I. Kornev, R. Ramesh, L. Bellaiche, L. Q. Chen, and S. V. Kalinin, Nat. Phys. **8**, 81 (2012).
[45] B. J. Rodriguez, X. S. Gao, L. F. Liu, W. Lee, I. I. Naumov, A. M. Bratkovsky, D. Hesse, and M. Alexe, Nano Lett. **9**, 1127 (2009).
[46] M. G. Stachiotti and M. Speliarsky, Phys. Rev. Lett. **106**, 137601 (2011).